LANGMUIR

pubs.acs.org/Langmuir Article

Grain Crystallinity, Anisotropy, and Boundaries Govern Microscale Hydrodynamic Transport in Semicrystalline Porous Media

Quang N. Pham, Michael T. Barako, and Yoonjin Won*

Cite This: *Langmuir* 2024, 40, 39−51 Read Online

ACCESS | Metrics & More | Article Recommendations | Supporting Information

ABSTRACT: Polycrystallinity is often an unintended consequence of real manufacturing processes used to produce designer porous media with deterministic and periodic architectures. Porous media are widely employed as high-surface conduits for fluid transport; unfortunately, even small concentrations of defects in the long-range order become the dominant impediment to hydrodynamic transport. In this study, we isolate the effects of these defects using a microfluidic analogy to energy transport in atomic polycrystals by directly tracking capillary transport through polycrystalline inverse opals. We reveal—using high-fidelity florescent microscopy—the boundary-limited nature of flow motions, along with nonlinear impedance elements introduced by the presence of "grain boundaries" that are separating the well-ordered "crystalline grains". Coupled crystallinity, anisotropy, and linear defect density contribute to direction-dominated flow characteristics in a discretized manner rather than traditional diffusive-like flow patterns. Separating individual crystal grains' transport properties from polycrystals along with new probabilistic data sets enables demonstrating statistical predictive models. These results provide fundamental insight into transport phenomena in (poly)crystalline porous media beyond the deterministic properties of an idealized unit cell and bridge the gap between engineering models and the ubiquitous imperfections found in manufactured porous materials.

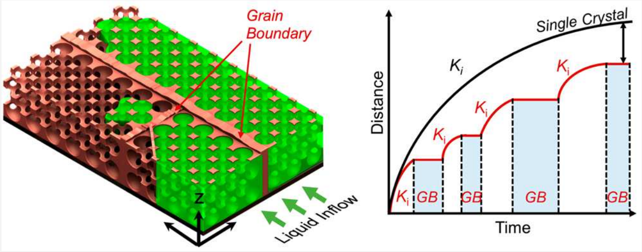

INTRODUCTION

A crystalline porous medium is a material with an ordered morphology defined by a lattice of repeating porous unit cells. The intrinsic pore shape and size of the base unit cell can be systematically engineered to achieve predictable and tunable transport properties in the macroscale crystalline porous superstructure. This level of precise structural definition is often inaccessible to conventional amorphous porous media such as foams,[1−6] bijels,[7−9] and fibrous networks[10−12] with a stochastic distribution of features, dimensions, and fluid pathways. Conventional manufacturing techniques for such amorphous porous media such as emulsification,[13,14] particle sintering,[15] layer-by-layer deposition,[5] templated electrodeposition,[16] and electrospinning[17] tend to produce disordered morphologies with minimal long-range order. These amorphous porosities are generally approximated using statistical descriptors of polydisperse structural features, and it is challenging to model transport and establish the rigorous structure−property relations necessary for material optimization. This significantly reduces the accessible engineering design space for porous media and limits the accuracy and utility of predictive transport models. By transitioning from stochastic to deterministic porous architectures, crystalline porous media can be rationally designed to achieve significantly higher rates of thermal and electrical conduction, capillary and forced mass flow, interfacial exchange, and liquid−vapor heat transfer compared to conventional porous media.

Porous media with long-range periodicity can be produced using emerging manufacturing techniques that include advanced lithography,[18−20] additive manufacturing,[21] and self-assembly.[22−32] While there have been tremendous efforts to approach defect-free crystallinity, most engineered porous media with long-range order contain a nonzero defect density due to nanoscopic perturbations, process variance, and imperfections in the fabrication process by changing their fabrication parameters.[22−24] These materials are categorized as polycrystalline porous media and are defined by morphologies with discrete domains of porous crystallinity with long-range order, or "grains", that intersect at "grain boundaries", as showcased in Figure 1.[25] Much like solid state transport in an atomic polycrystal, hydraulic transport in a polycrystalline microporous medium is determined by the summative effects of transport within the crystalline domains and transport across the grain boundaries. While hydraulic transport in well-defined

Received: May 14, 2023
Revised: October 4, 2023
Accepted: October 4, 2023
Published: December 4, 2023

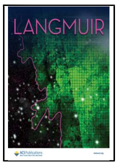

https://doi.org/10.1021/acs.langmuir.3c01276

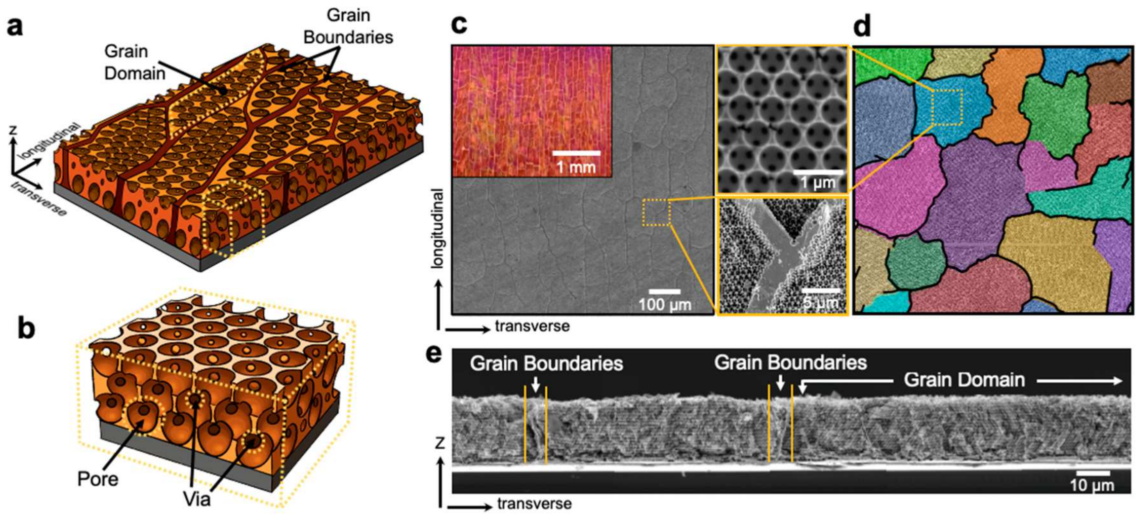

Figure 1. Polycrystalline inverse opal, an example of polycrystalline porous media. (a) Illustration of inverse opals (IOs) with naturally occurring boundary barriers separating (b) crystalline domains of uniform spherical pores, interconnected in a three-dimensional lattice superstructure by adjacent windows, denoted as "vias". (c, d) Scanning electron microscopy (SEM) stitched images of IOs from plan view, displaying grain boundaries and the regularity of pore arrangement. The polycrystalline nature of copper IOs can be optically observed in the inset of (c). (d) The false color overlay indicates the polycrystallinity of IOs, while the black lines follow the contours of grain boundaries. (e) Cross-sectional stitched SEM images show that the grain boundaries fully extend along the thickness of the IO, demarcating each IO domain.

geometries can be predicted with relatively high accuracy using numerical simulations, grain boundaries introduce flow field complexities that are significantly more challenging to model while potentially having a significant impact on the collective transport characteristics of the porous medium.

■ EXPERIMENTS

Inverse opals (IOs) exemplify the three-dimensional pore-matrix architecture, where monodisperse spherical pores contact adjacent pores at well-defined points in a crystalline lattice. IOs are manufactured through a self-assembly templating process.[33−36,37−40,41] First, a three-dimensional colloidal crystal (an "opal") is synthesized by self-assembly of suspended nanospheres ($\sim 10^{-1}-10\ \mu$m) in an evaporating solvent. Despite the opal's natural tendency to spontaneously arrange into crystalline formation,[33] long-range periodicity ($>10^2$ periods) is often disturbed by the introduction of nanoscopic defects and perturbations during the fabrication process. These defects include nonuniform intrinsic characteristics (e.g., sphere polydispersity) and extrinsic conditions (e.g., solvent evaporation rate), which facilitate the formation of microscopic defects between ordered domains and often manifest as propagated cracks in the crystal.[22−25] By backfilling these cracks in the opal templates with a structural material (i.e., polymer or metal) during inversion,[34−36,41] these cracks become barriers, or "grain boundaries", as displayed in Figure 1, while other types of defects like tilt-twist configurations in the opal can be transformed into impermeable walls, affecting aspects like wall thickness and defect severity. Even the grain boundaries in polycrystalline IOs present hydraulic impediments that can become the dominant impedance to capillary mass transport between porous domains.[25,42−44] While capillary transport within a perfect, crystalline IO unit cell can be readily modeled using finite elements due to exact knowledge of geometry and symmetries,[25,45,46,47] hydraulic transport in a polycrystalline IO superstructure requires more detailed knowledge of the underlying transport physics in the presence of grain boundaries.

Grain boundaries in polycrystalline porous media negatively impact energy and momentum transfer through the structure.[25] This interaction influences the flow field and local velocity of the fluid that, even in small concentrations, can reduce the capillary performance parameter by more than an order of magnitude. In such cases, the engineering advantages of the carefully designed and/or optimized porous architecture become overwhelmed by the presence of defects in the fabricated material. We show that these boundaries can be represented as hydraulic impedance elements connecting Darcian regions of high permeability in a composite network model. While grain boundaries introduce an impediment to capillary wicking, the propagating nature of the liquid front often flows discretely in the presence of these obstructions. For example, the liquid front propagates across the crystalline grains of porous media and momentarily pins at each grain boundary before the adjacent capillary-filled domains enable the liquid front to overcome the boundary impedance. In other cases, the liquid front remains pinned behind the grain boundary but is able to overcome the barrier after a certain amount of time has elapsed, wicking in a stop-and-go manner across multiple polycrystalline porous domains. To understand these microscopic liquid propagation behaviors in polycrystalline porous media, the capillary driving forces within the intrinsic porous crystallites must be dissociated from the effects of the grain boundaries. While we explore these effects using IOs as a model porous medium, it is expected that the same fundamental transport physics and interpretations would apply to other periodic porous media for capillary flow.

In this study, we elucidate the fundamental physics governing liquid propagation in polycrystalline IOs through capillary-driven transport. Using high-fidelity fluorescence microscopy, we quantify the hydraulic impedance of grain boundaries with respect to the capillary-driven liquid flow vector, which depends on structural characteristics, coupling grain crystallinity, orientation of the grains and grain boundaries, and linear defect density. We then correlate the measured two-dimensional liquid propagation profile to a high-

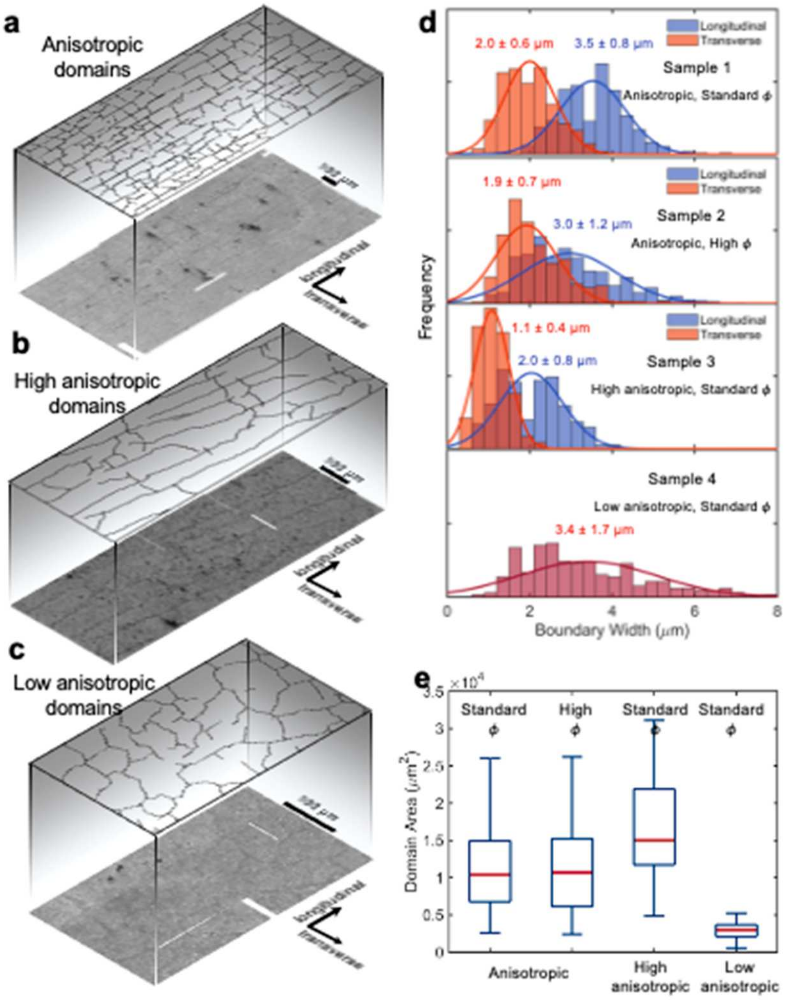

Figure 2. Grain domain and boundary characteristics. Representative schematic outlines of grain boundaries projected from plan view SEM image stitching of samples 1, 3, and 4 with (a) anisotropic, (b) high anisotropic, or elongated, and (c) low anisotropic, or isotropic domains, respectively. Note that samples 1 and 2 exhibit similar domain characteristics; therefore, grain boundary projections are presented only for sample 1. (d) Normalized frequency distribution of grain boundary widths as collected from a minimum of 500 measurements and (e) boxplot of grain domain area for IOs with various domain characteristics and porosities. The amorphous structure in sample 5 lacks crystalline characteristics, and no grain boundaries or domain characteristics are available for the analysis.

resolution microstructural map of the IO domains to reveal the underlying physics of boundary-limited transport through polycrystalline porous media. The empirically driven statistical data sets can be corroborated with a predictive model that accounts for the probabilistic nature in the parameters.

Structural Characteristics. As the representative polycrystalline porous media, copper-based IOs are fabricated using a combination of self-assembly of monodisperse polystyrene microspheres to form an opal template with deliberate disturbances during the manufacturing process to induce defects and other structural irregularities, electrodeposition of copper between the void volumes of the opal, and subsequent selective removal of the template (see Materials and Methods).[25,26] In this study, uniform spherical pore diameters of 0.6 μm are fully interconnected by adjacent windows (“vias”) to present a close-packed, crystalline arrangement of pores in a three-dimensional lattice superstructure.

Five sets of design parameters of IOs are carefully selected to systematically tune their physical construction (by exploiting the self-assembly of the microspheres during the templating process; see Materials and Methods) and thus explore their associated transport properties of samples 1−5. These tunable descriptors examined can be defined as the following: (i) crystallinity describes the pore-packing quality and can be defined as being crystalline (long-range periodicity) or amorphous (unit cell disorder); (ii) domain shape describes the general crystallite shape based on the intersectional layout of grain boundaries (e.g., anisotropic, elongated, or isotropic); (iii) anisotropy can be described as the ratio of the crystallite length Λ_L and width Λ_W (e.g., $\Lambda_L/\Lambda_W \approx 1$ is “isotropic”, $1 \leq \Lambda_L/\Lambda_W \leq 3$ is “anisotropic”, and $\Lambda_L/\Lambda_W > 3$ is “elongated”); (iv) porosity can be tuned within the range of the close-packed point-contact model (~74%) and the upper limit for a continuous scaffold (~96%).[29,48]

The structural descriptors of samples 1−5 are quantified with SEM images. Stitching high-resolution top-view SEM images of the sample provides a microstructural map that can be correlated to the fluorescence map during capillary saturation. The outlines of grain boundaries projected from the SEM mappings are shown in Figure 2a−c. Using these images, we quantify the grain boundary width W_{GB}, grain domain area, as displayed in Figure 2d,e, and the lengths Λ_L

Table 1. Structural Characteristics of Inverse Opal Samples

sample	crystallinity	domain shape	anisotropy Λ_L/Λ_W	porosity ϕ (%)
1	Polycrystalline	Anisotropic	2.4 ± 1.3	Standard, 78.0 ± 5.8
2			2.1 ± 0.9	High, 90.9 ± 2.4
3		High anisotropic or elongation	3.3 ± 1.6	Standard, 80.3 ± 3.2
4		Low anisotropic or isotropic	1.1 ± 0.3	Standard, 79.0 ± 6.3
5	Amorphous	Amorphous		Low, 52.7 ± 8.7

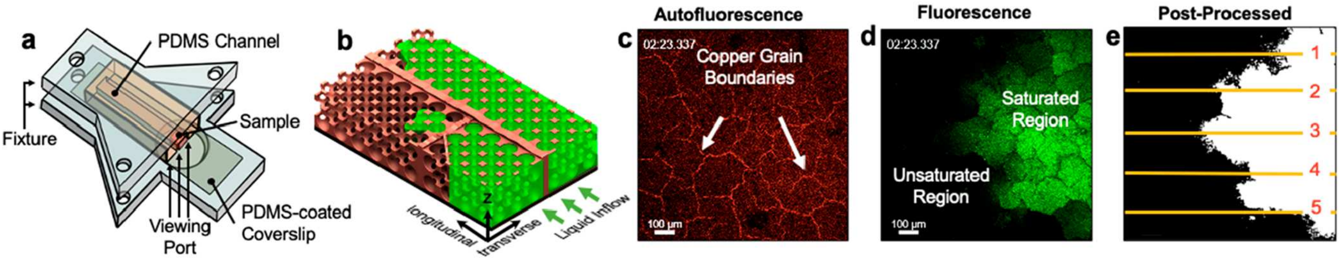

Figure 3. Liquid propagation data collection via fluorescence microscopy imaging. (a) An acrylic fixture sandwiches the IO sample between a PDMS-coated glass coverslip and a PDMS gasket with a rectangular channel. The fixture is placed onto an inverted confocal microscope equipped with fluorescence imaging. (b) The fluorescence liquid propagating through the IOs is excited and observed through the viewing port, with liquid inflow occurring from left to right. The rendering depicts liquid flow in the longitudinal direction. Representative frame captures from (c) autofluorescence channel showing the copper IO and its grain boundaries with isotropic-dominated domains, (d) fluorescence channel displaying liquid (green) saturating the IO, and (e) post-processed image showing the propagated liquid front being detected along five equidistant markers (yellow lines) for IOs.

and widths Λ_W of grain domains where the anisotropy ratio Λ_L/Λ_W describes the degree of domain anisotropy. Cross-sectional SEM imaging confirms that the IO thickness is approximately 15 μm for all samples.

For each sample, we measured the diameter of the vias between pores using high-magnification SEM images from at least 150 measurements. By assuming the pore diameter is equal to the self-assembled sphere size (0.6 μm, see Supplementary Figure 1), we then compute the porosity which, for a face-centered cubic IO, is uniquely defined by the relation

$$3\phi = 1.75 d_{\mathrm{via}}/d_{\mathrm{pore}} + 1.99 \quad (1)$$

where d_{via} and d_{pore} are the diameters of the via and pore, respectively.[25] The resulting structural descriptors are presented in Figure 2 and Table 1 (with full statistics presented in Supplementary Figure 1) and are correlated to their transport properties in a later section.

Design of Experiments: Liquid Transport Data Collection via Fluorescence Microscopy Imaging. To understand liquid propagation physics in porous media at the microscale, the capillary-driven flow has often been visualized using traditional stereomicroscopy or high-speed imaging.[49,50,51,52,53−56] These techniques present weak contrast in the transition between saturated and unsaturated regions, making it challenging to discern with high spatial fidelity and confidence the exact location of the liquid front. Fluorescence microscopy has become an essential tool in biology and biomedicine in detecting cells and nanoscopic cellular components with a high degree of specificity, contrast intensity, and temporal resolution compared to traditional microscopy. Rather than tracking the optical changes induced by the wetting of the fluid, we track the spatial−temporal signature of fluorophore markers contained in the liquid, foregoing the need to resolve the subtle optical changes induced by the carrier fluid.

In this study, the dynamics of in-plane liquid propagation through the polycrystalline IOs are microscopically monitored using a custom-designed setup compatible with a fluorescence microscope. Figure 3a shows the schematic of the custom fixture that is used to seal the IOs while allowing their capillary-assisted wicking behaviors to be monitored. The fluorescein-infused water wets the copper IO media with capillary-driven flow saturating porous grain domains while mass transport is throttling across grain boundaries (Figure 3b). By isolating the individual fluorescing channels (i.e., the fluorescence channel for the propagating liquid and the autofluorescence channel for the copper IO structure, as shown in Figure 3c,d), the liquid propagation front is clearly discernible. This ability to precisely locate the liquid front with strong spatial contrasts and high specificity using the employed fluorescence technique is a significant advantage over the ambiguity often associated with conventional optical microscope measurements. The strong spatial contrasts of the liquid front allow effective image binarization during image processing to identify the saturated and unsaturated regions from each frame. The time-varying propagation distances at pixel resolution are recorded along equidistant lines using postprocessing computer detection (see Figure 3e for representative post-processed images with five lines) and presented as spatiotemporal plots to display variances in propagation behaviors over spatial and time coordinates (Figure 4 and Supplementary Figures 2 and 3). The fluorescence images are then aligned and overlaid onto the stitched scanning electron microscope (SEM, FEI Quanta 3D) images of each polycrystalline IO to correlate the high-contrast liquid transport with the high-fidelity microstructural map. The relationships between the localized physical boundary structure and the concurrent liquid propagation dynamics are correlated to elucidate underlying structure−transport properties. For instance, a propagating front may saturate an entire domain but can be stopped at a grain boundary before eventually proceeding to circumvent it. By correlating such grain-scale events with a microscopic mapping of the IO, the observed

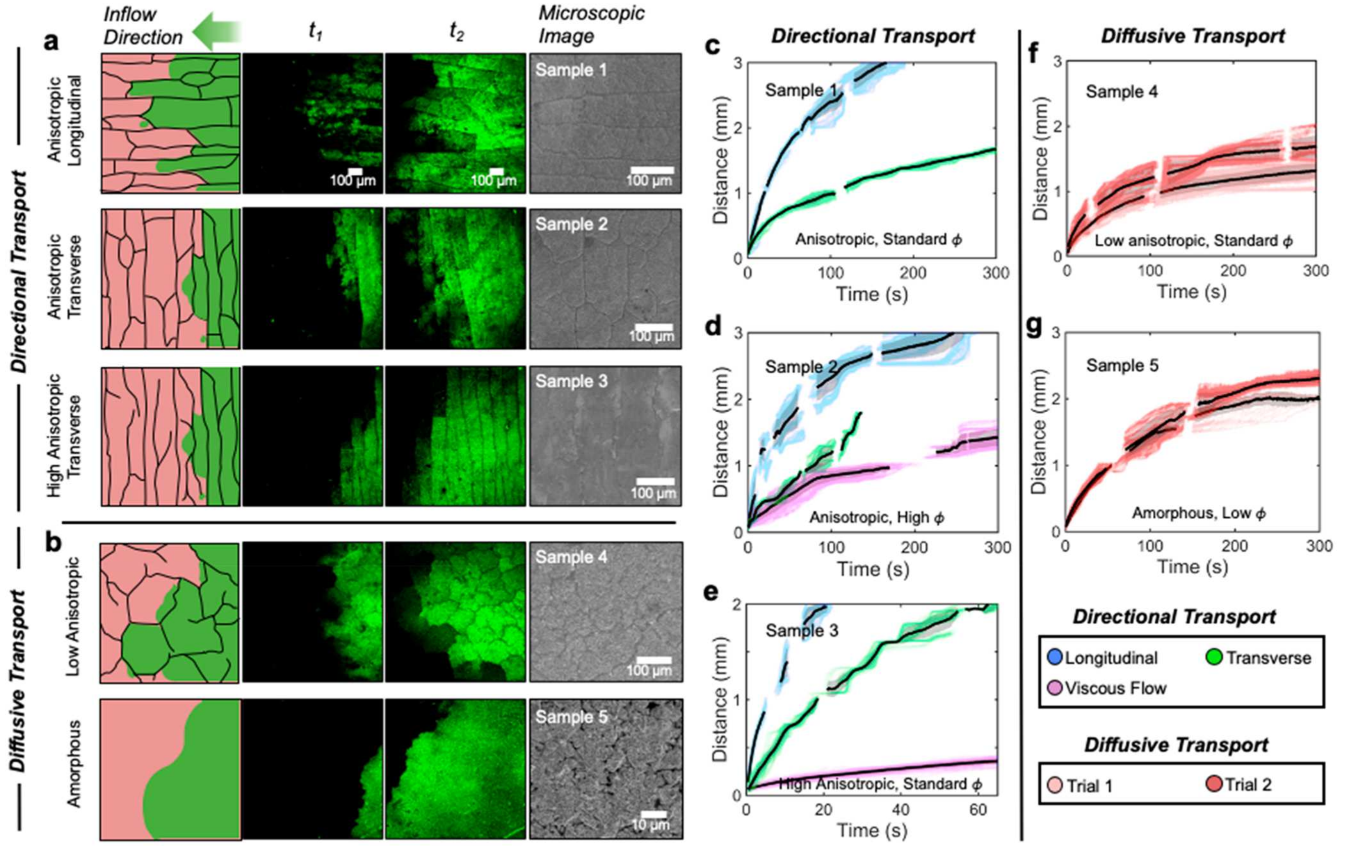

Figure 4. Liquid propagation across IOs with various design of experiments. The different flow configurations are represented through schematic illustrations, fluorescence frame captures of liquid propagation over time, and representative plan view SEM images of the associated IOs. The microscale hydrodynamic phenomena can be categorized based on their (a) directional and (b) diffusive transport characteristics. The propagating liquid front is plotted for directional transport, (c) anisotropic with standard porosity, (d) anisotropic with high porosity, (e) high anisotropic, elongated domains (samples 1−3, respectively), as well as diffusive transport, (f) low anisotropic, isotropic, and (g) amorphous domains (samples 4 and 5, respectively). (c−e) The propagating liquid fronts are displayed as a culmination of overlapping colored lines that display a band range based on the flow directions (blue, longitudinal; green, transverse; magenta, longitudinal for viscous fluid). It should be noted that (d) has a terminal propagating distance limited by the sample size (∼2 mm). (f, g) To demonstrate the limited effect of directionality in flow behaviors, the samples are rotated by 90° between capillary-assisted transport measurements (red, trial 1; pink, trial 2). The minor disparities between trials can be attributed to the nonuniform degree in domain isotropy (for sample 4) and the heterogeneity in the randomly packed pores (for sample 5). This might be related to sample degradation due to remnants of fluorescence or oxidation upon contact with air. The plotted black lines represent the mean of the pixel-based data, and the translucent gray bands represent the standard deviations. (c−g) It should be noted that data recording becomes discontinuous in the event of a viewing window shift during measurements, concurrent with the ongoing wicking process; see Supplementary Figure 3.

transport characteristics of each grain boundary can be determined with specificity and locality.

To identify different flow characteristics, we carefully review and determine the design of experiments that vary both flow directions and working fluids: (i) Two directions will be used to examine the effect of flow vectors on the fluid propagation behaviors, by rotating the sample by 90° between each measurement for each sample, and (ii) fluid viscosities including standard viscous fluid (i.e., water) and high viscous fluid (i.e., dextran-based fluid) will be tested to exploit the impact of fluid viscosity on boundary-limited transport mechanisms. Further details regarding the setup are outlined in Materials and Methods, Supplementary Table 1, and Supplementary Figures 2 and 3. The following liquid propagation results are shown in Figure 4 and Supplementary Figure 4.

■ RESULTS AND DISCUSSION

Directional Hydraulic Transport through Anisotropic Porosity. Due to the directionality of the opal self-assembly during vertical deposition, grain domains often exhibit anisotropic structural characteristics. These grains tend to be elongated and are bounded by prominent longitudinal (aligned to the direction of the moving meniscus) and transverse grain boundaries (orthogonal to the direction of the moving meniscus). To exploit the domain anisotropy and its influence on direction-dominated flow, we measure capillary flow through IOs that are anisotropic (either standard or high porosity; samples 1 and 2, respectively) and elongated, high anisotropic domains (sample 3). The sample orientation illustration, associated fluorescence evolutions, and top-view SEM image are shown in Figure 4a, exhibiting directional flow characteristics.[57,58]

The wicking results in Figure 4c−e demonstrate that domain anisotropy induces 2−3 times faster propagation rates along the prescribed longitudinal direction (blue lines) compared to the transverse direction (green lines), indicating a preference in the directionality of the flow vector. The faster liquid propagation along the longitudinal direction is indicative of the lower hydraulic impedance expected for a reduced linear density of grain boundaries.

Despite the differences in porosity for sample 1 (anisotropic, standard porosity) and sample 2 (anisotropic, high porosity), the statistical population of other structural characteristics (i.e., the porous domain area, grain boundary density, and transverse grain boundary width) is almost identical (Figure 2a,d,e). This may explain their similar propagation rates along the longitudinal direction (blue spatiotemporal plots in parts c and d of Figure 4, respectively). In comparison to sample 1, sample 2 possesses 17% smaller longitudinal boundary widths, which allows it to propagate at a faster rate in the transverse direction by approximately 20% (green spatiotemporal plot in Figure 4c,d). This suggests that the grain boundary widths correlate with the amount of hydraulic impedance posed by the barriers in throttling the fluid propagation. Furthermore, when grain boundaries are the dominant limiting factors in transport performance, the intrinsic properties of the IOs (e.g., porosity) do not exhibit as strong of an impact on transport physics. Instead, the anisotropic layout of the porous domain has been demonstrated to be more prominent in influencing the nature of propagation, such as discretized and delayed stop-and-go motion, preferential directional transport, and the overall wicking rate through the crystalline porous media.

The study of directional transport is extended to high anisotropic domains (sample 3; high anisotropic, standard porosity). Compared to the anisotropic IOs (samples 1 and 2), the boundary widths of sample 3 are much smaller in either direction (Figure 2d) while its domain areas remain the largest (Figure 2e). The increase in crystalline domain areal coverage indicates a reduction in grain boundary density, as visually corroborated with the boundary outline projection displayed in Figure 2b. The microstructural map also reveals that most boundaries are loosely connected such that domains have direct access between grains as opposed to being truly isolated, causing the effective permeability to remain high. The wicking fluid circumvents around boundaries by finding openings between domains with more ease, decreasing the residence time during fluid confinement behind grain boundaries. The combinations of lower grain boundary density, smaller boundary widths, and more grain-to-grain connections reduce the modes of hydraulic impedances and thus a 3-fold increase in propagation rate over the previous anisotropic IOs (Figure 4e).

Diffusive Hydraulic Transport through Isotropic and Amorphous Porosity. By eliminating the anisotropy in the crystalline domain shape, the preferential limit to direction-dominated transport can be investigated. For this, we create isotropic periodic porous media (sample 4; low anisotropic, standard porosity) and amorphous pore packing (sample 5; amorphous, low porosity) by modulating the manufacturing process of IOs, as shown in Figure 2c. The associated flow characteristics exhibit diffusive-like propagation behaviors with no preferences for directionality. This is evident from the spatiotemporal plots in Figure 4f,g, showing samples 4 and 5 exhibiting similar propagation behaviors between trials of 90° sample rotation (red and pink lines, respectively). As observed from the detailed fluorescence imaging (Figure 4b), the fluid propagation behaviors through sample 4 diffuse in all directions in a discretized manner at grain boundaries, which is the boundary-limited transport, whereas the fluid in sample 5 propagates and diffuses in a smooth and continuous manner.

In detail, the grain boundary width of sample 4 widely ranges (Figure 2d), and its domain area is at least 5 times smaller than the other IO samples (samples 1−3; Figure 2e), indicating the prominence of defects. A high defect density of sample 4 results in slow capillary wicking at a rate similar to that of sample 1 (anisotropic, standard porosity) in the transverse direction, which is the slowest among all samples and directions when the standard viscous fluid is applied (Figure 4c). While the lack of boundary defects in sample 5 indicates less hydraulic impedance density, the randomly packed pores (often non-interconnected pores) create extremely tortuous permeable pathways that dramatically increase hydraulic impedance across the medium. The high tortuosity of sample 5 induces a comparable transport rate as the grain boundary-dense sample 4.

Overcoming Boundary-Limited Transport. The effective hydraulic impedance thus far is understood to be the summation of the intrinsic capillary impedance induced by grain boundaries.[44] However, by increasing the fluid viscosity for a given sample, we also contribute to a relative increase in Darcian hydraulic impedance, since[59]

$$U_m = -\frac{K}{\mu}\frac{dP}{dx} \tag{2}$$

where U_m is the Darcy mean velocity through a porous medium, K is the permeability of the medium, dP/dx is the pressure gradient, and μ is the dynamic viscosity. We use a dextran-based fluid to increase the viscosity by 2 orders of magnitude and measure the wicking in the longitudinal direction for samples 1, 2, and 3 (Figure 4d,e).

It should be noted that propagation of high viscous fluid stops within less than ∼0.1 mm due to insurmountable flow impedance within sample 1 (anisotropy and standard porosity) and thus is not presented. Sample 2 (anisotropy, high porosity) previously demonstrated the second fastest wicking rate using standard viscous fluid behind sample 3 (high anisotropy, standard porosity) but became fastest under the high viscous fluid. The previous rapid propagation of sample 3 can be attributed to its lower defect density. In contrast to this, however, with a significant increase in fluid viscosity, transport becomes relatively more efficient in media with higher porosity that provide more open permeable pathways. Since the liquid viscosity induces friction between the moving fluid and the solid surfaces, a higher porosity provides fewer opposing forces to the fluid movement. While grain boundaries contribute to a significant portion of hydraulic impedance under standard viscous flow conditions, the use of high viscous fluids supersedes the role of grain boundaries to become the dominant mode of hydraulic impedance, in which the structural porosity (rather than defect density) becomes the strongest influencing factor on the transport rate.

Microscopic Discretized Transport and Hydraulic Impedance across the Grain Boundaries. The prominent propagation characteristic observed in polycrystalline porous media is the discretized stop-and-go fluid motion between grain boundaries (for samples 1−4). During the discretized flows, the residence time that the liquid remains pinned at the grain boundaries can be denoted as Δt_{GB}, which reflects the

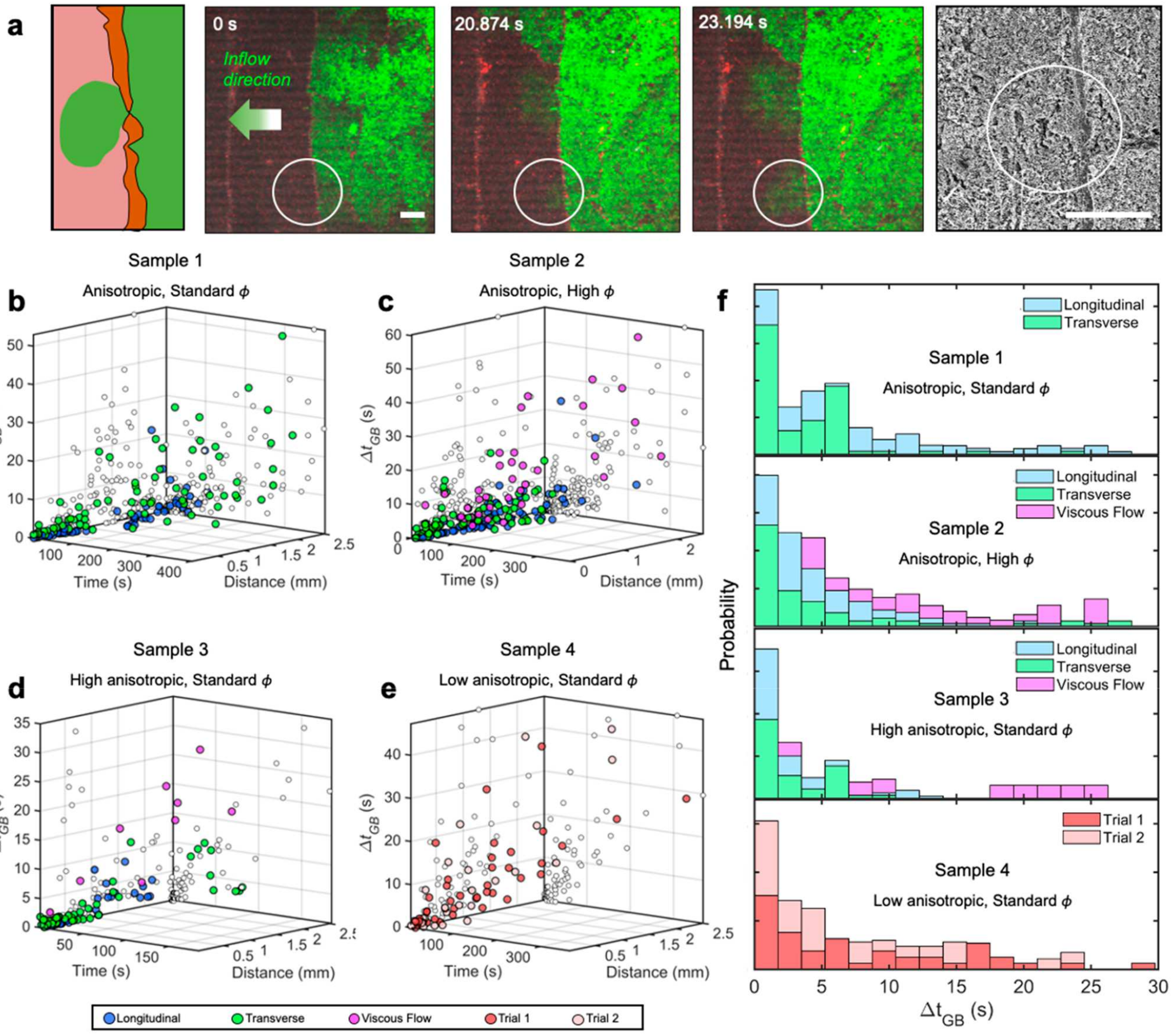

Figure 5. Discrete nature of hydrodynamic motions at grain boundaries. (a) Illustration of the series of fluorescent images over time, and SEM show that microscopic hydraulic motion mainly overcomes across grain boundaries through their own defective sites. All scale bars are 50 μm. Empirically measured Δt_{GB} as a function of propagation time and distance for (b−e) samples 1−4, respectively, with varying experimental designs. The two-dimensional correlations between Δt_{GB}, time, and distance are projected onto the axis planes to show Δt_{GB} versus distance and Δt_{GB} versus time. The results indicate that Δt_{GB} generally increases with time and distance. (f) Stacked histogram distributions of Δt_{GB} are shown for longitudinal (blue), transverse (green), and viscous flow (magenta) as well as diffusive-like flows (red and pink).

hydraulic impedance posed by the physical obstructions in relation to grain boundary characteristics (such as boundary defects, density, width, and grain-to-grain connections) as well as the propagation process. There might be multiple physical mechanisms to overcome the hydraulic impedance, which include bursting effects (with the existence of pinning of the meniscus at a sharp edge), lateral wicking (goring around the boundary), and partial permeability of the boundary. The discretized flow characteristics are shown in Supplementary Figure 5.

One mechanism to overcome the hydraulic impedance is to cross grain boundaries through their own defective sites and discontinuities, after Δt_{GB}, as evidenced in Figure 5a and Supplementary Figure 6. Through a detailed SEM examination of localized sites where fluorescein signatures cross grain boundaries, we reveal that the boundary possesses minor defects along its length, such as discontinuities along the barrier and nonuniformity in grain boundary width and height, allowing the liquid to propagate across defective sites with minimum flow impedance. Atomic force microscope (AFM) scans of grain boundaries show that their heights can vary by 1 μm (Supplementary Figure 7); SEM images confirm boundary widths can drastically narrow or pinch off. Detailed characterizations and analysis of microscopic transport across boundaries are presented in Supplementary Figures 6 and 7 and Supplementary Note 1.

The microscopic transport through submicrometer scale defects occurs as a result to minimize the surface energy of the IO; a molecular liquid film that propagates ahead of the saturating film coats the grain boundaries and eliminates the liquid−vapor interfaces across the physical obstructions[60] (given that the boundaries themselves are hydrophilic to support surface wetting). The molecular liquid film propagation over the boundaries is driven by the energy obtained from the wicking liquid filling the porous domains between boundaries. Thus, we often observe that while the saturation front may be inhibited behind grain boundaries, after a certain amount of Δt_{GB} as the liquid completely saturates the porous domain in three dimensions (as confirmed by the increasing intensity of the green fluorescence signals within the trapped domain over time), the wetting liquid front is eventually propelled to cross and diffuse into the adjacent domain through boundary defects.

Despite the compounding hydraulic impedances by multiple grain boundaries, the liquid continues to propagate across the defects after a finite Δt_{GB}. However, the momentum and pressure to overcome grain boundary defects decrease, Δt_{GB} thereby generally increases with time and distance away from the liquid source, as displayed in Figure 5b−f and Supplementary Figure 8. By developing multivariable correlations of $\Delta t_{GB}(h,t)$ through linear regression, we can predict the residence time over the duration of wicking event, which can be used as the input for the predictive model of discretized, boundary-limited flow motions.

Crystalline Grains and Polycrystals. The overall capacity to transport the fluid is described by the permeability of the porous medium. The permeability K can often be associated with fluid propagation rate across the medium, using the Washburn equation:

$$h^2 = \frac{4\sigma}{\mu\phi}\frac{K}{r_{\mathrm{eff}}}t \qquad (3)$$

where h is the propagation distance as a function of time t, σ is the surface tension, ϕ is the porosity, and r_{eff} is the effective pore radius described as $r_{\mathrm{eff}} = 0.5\, d_{\mathrm{pore}}/\cos\theta$, where θ is the apparent contact angle. Unlike the discretized fluid propagation in porous polycrystals, the Washburn equation (eq 3) describes a continuous and smooth fluid advancement by assuming homogeneous porous media (i.e., without grain boundaries or other discontinuities). Our phenomena depict partial or increasing saturation, resulting in the variation of the capillary pressure in microstructures. By considering this variation might be small enough, the Washburn equation has been used to describe mesoscopic liquid propagation and find a way to represent the liquid wicking through microstructures.

Based on this equation, we can separately define an intrinsic permeability K_i within each single crystalline grain while establishing a separate effective permeability K_{eff} term for the aggregate polycrystals to deconvolute the effects of grain boundaries. Using eq 3, we determine K_i by measuring the liquid saturation of individual grains. To validate our approach, we overlay the predicted discretized propagation rate onto the experimental data using the derived K_i intrinsic to each grain domain in Figure 6a, which provides consistent agreements. Figure 6b representatively shows that K_i significantly decreases the further the domains are from the liquid reservoir because of the compounding impedance from the increasing number of obstructions the fluid must traverse across. Our empirical measurements of K_i are at least 1 order of magnitude lower than computational models from an IO unit cell, and the value difference can be mainly attributed to the hydraulic impedances posed by grain boundaries.[25] For a given grain, K_i can vary drastically depending on the orientation of the anisotropic domains, such that propagation in the longitudinal direction (blue circle markers) generally remains 1 order of magnitude higher in K_i than in the transverse direction (green circle markers) in Figure 6b. The direction-dependency of K_i manifests from the crystal travel length ($\Lambda_{L,i}$ or $\Lambda_{W,i}$) and linear defect density that change based on the direction of the flow vector.

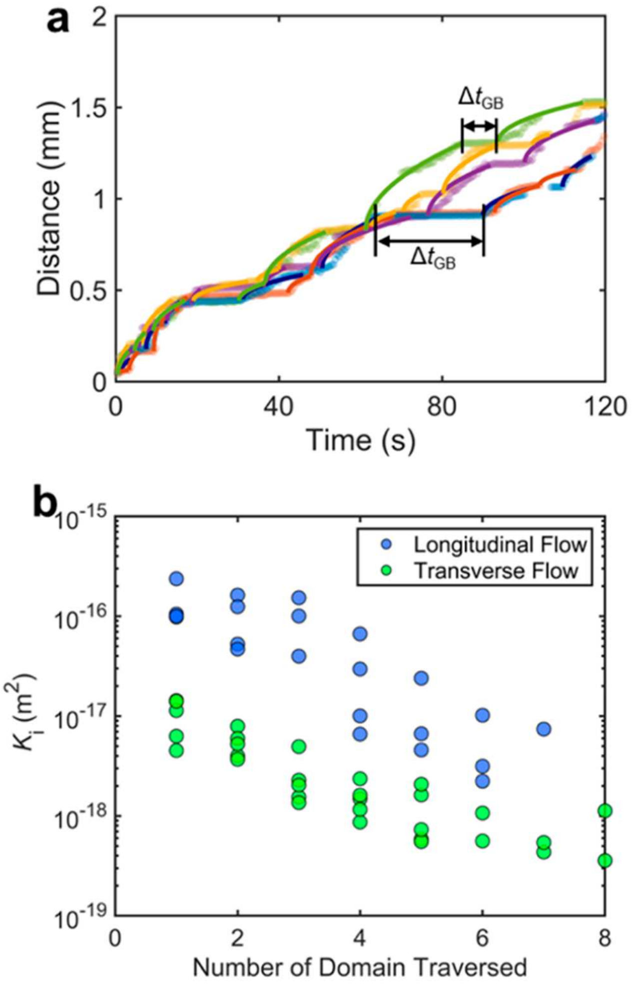

Figure 6. Intrinsic permeability of individual crystal grains. (a) Following the liquid propagation linearly along five equidistant sites, the liquid propagation is fitted using the intrinsic permeability K_i within single crystalline grains derived from the Washburn equation. The fitted data are solid colored lines, while the experimental measurements are transparent markers. The guided annotations showcase the stoppage in liquid propagation at grain boundaries where this residence time is denoted as Δt_{GB}. (b) Examining the liquid propagation along a series of multiple crystal grain domains and boundaries (for sample 2), K_i logarithmically decreases with an increasing number of domains and boundaries traveled across. Intrinsic permeabilities also differ by 1 order of magnitude between the longitudinal (blue markers) and transverse (green markers) flow directions.

The summative effects of K_i from individual grains and Δt_{GB} from grain boundaries contribute to an effective permeability K_{eff} of the IO superstructure. This suggests that the value of K_{eff} is a nonconstant that depends on the linear defect density along the fluid propagation pathway. By considering both the capacity and impedance to transport, we determine K_{eff} for each sample and flow vector, which we demonstrate reasonable agreements with the measured propagation results (Supplementary Figure 9 and Supplementary Note 2).

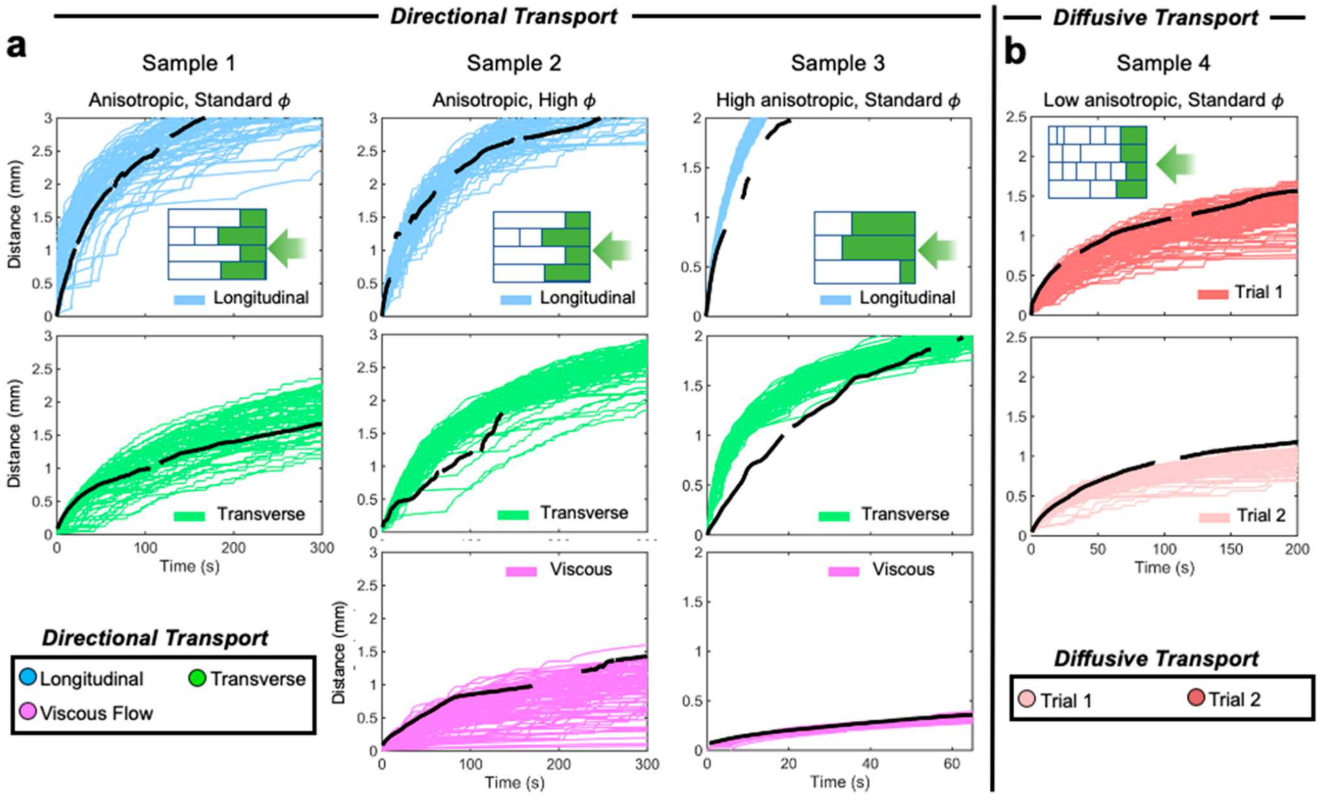

Figure 7. Predictive models of boundary-limited hydraulic transport via Monte Carlo simulations. Based on the normalized probability distribution of empirical-derived parameters as inputs, the predictive models (color lines) using Monte Carlo simulation are demonstrated for each sample and agree with the averaged empirical data sets (black lines) within 85−95% for both (a) directional and (b) diffusive transport.

Predictive Model for Boundary-Limited Hydraulic Transport: Monte Carlo Simulations. While the Washburn equation describes the hydraulic transport in homogeneous media, we extend it to derive an expression for porous polycrystals based on the statistical distribution of features and summative effects of hydraulic impedance. To construct the generalized solution to predict boundary-limited fluid flow, we create a simplified model of polycrystalline porous media (see Supplementary Figure 10) such that an individual crystalline grain i possesses an intrinsic permeability $K_i(h)$ (that varies as a function of propagation distance h) as well as a boundary-to-boundary travel length Λ_i ($\Lambda_{L,i}$ or $\Lambda_{W,i}$ depending on the direction of the flow vector). To describe the total propagating distance h_{tot}, we sum the individual grain working distance h_i, which includes the travel length Λ_i and the grain boundary width $W_{GB,i}$ over a specified number of crystalline grain N:

$$h_{tot} = \sum_{i=1}^{N} h_i = \sum_{i=1}^{N} (\Lambda_i + W_{GB,i}) \tag{4}$$

We then modify the Washburn equation (eq 3) to predict the total propagation time t_{tot} by considering the propagation time within a single crystalline grain i and the residence time at a grain boundary adjacent to the crystalline grain:

$$t_{tot} = \sum_{i=1}^{N} t_i(h) = \sum_{i=1}^{N} \left(\frac{\mu\phi}{4\sigma} \frac{r_{eff}}{K_i(h)} \Lambda_i^{\ 2} + \frac{W_{GB,i}}{\overline{W_{GB}}} \Delta t_{GB,i}(h,\ t) \right) \tag{5}$$

where $\overline{W_{GB}}$ is the mean grain boundary width over multiple crystalline grains, as presented in Figure 2d. Therefore, the modified Washburn equation (eq 5) can capture the effective transport properties of porous polycrystals, as described by the summation of their discretized fluid propagation events. In this equation, since $K_i(h)$ and $\Delta t_{GB}(h,t)$ vary over propagation distance (and time), correlations are fitted to these empirically derived data (Figure 5b−f) and are then used to determine their realistic values based on their spatial and temporal coordinates during the propagation.

The discretized nature of microscopic flow through polycrystalline porous media can be modeled using non-weighted Monte Carlo simulations, by using a stochastic and probabilistic approach to converge upon realistic liquid propagation behaviors. The simulations are executed by randomly sampling the known structural characteristics (such as the normalized probability distribution of Λ_i (Supplementary Figure 1) and correlations (such as $K_i(h)$, and $\Delta t_{GB,i}(h,t)$) based on the modified Washburn equation (eq 5). The demonstration of an extensive number of simulation iterations identifies various possible propagation outcomes and their likelihood. The simulations closely resemble that of empirically observed behavior (Figure 7) with errors ranging between ~5% and ~15% in most cases due to the high sensitivity and statistical variation in the stochastically generated input states. This confirms that the convergence and predictivity of Monte Carlo simulations obtain the numerical solutions that can describe three-dimensional, propagation physics with a relatively high level of certainty, while our modified Washburn model considers fluid flow only in one dimension in a three-dimensional porous polycrystal.

■ CONCLUSIONS

The use of a new classification of porous materials through three-dimensionally ordered microporous structures advances the understanding of the flow characteristics within polycrystalline porous structures. Boundary-limited, discretized hydraulic transport behaviors through polycrystals are presented here because of the hydraulic impedance of crystalline defects or grain boundaries in the flow pathway. Central to the flow characteristics are the grain and boundary structures. As demonstrated in Figure 8, porous designs consisting of defect-free, large crystal grains show boundary-free hydrodynamic transport while the porous structures coupled with grain crystallinity, anisotropy, and linear defect density can contribute to direction-dominated flow characteristics in a discretized manner. Contrarily, isotropic or amorphous porous media present traditional diffusive-like flow patterns, where the grain boundary effects on transport can be engineered by varying fluid viscosity. We then separately identify the transport of individual crystals and establish an analytical model for hydraulic transport in polycrystalline porous media by modifying the traditional Washburn equation. The statistical data sets of structural characteristics along with the distribution of empirical-derived parameters enable building predictive Monte Carlo models that account for probabilistic data sets. While our findings here elucidate the hydraulic transport physics using inverse opals as a representative polycrystalline porous medium, the fundamental transport physics and interpretations are applicable to describe capillary-based transport in other periodic porous media exhibiting physical defects and obstructions.

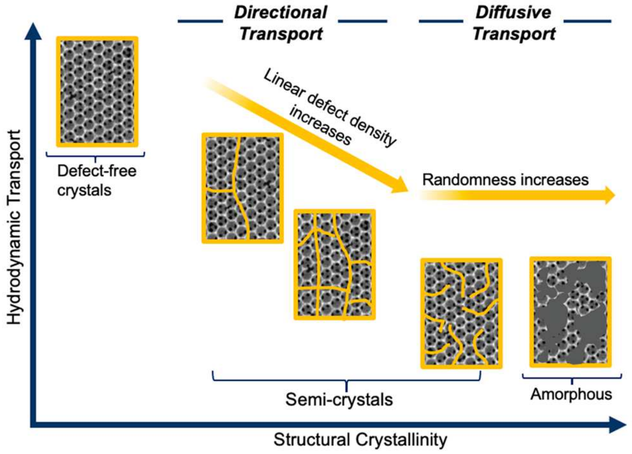

Figure 8. Regime map showing grain crystallinity effects on hydrodynamic transport. Flow characteristics through porous media are centered on the design of porous materials that are responsible for grain crystallinity and grain boundaries. Coupled grain crystallinity, anisotropy, and linear defect density can contribute to direction-dominated flow characteristics in a discretized manner rather than traditional diffusive-like flow patterns within isotropic or amorphous porous media.

■ MATERIALS AND METHODS

Copper Inverse Opal Fabrication. Copper-based IOs are fabricated using a combination of self-assembly template-assisted and electrodeposition process, with details presented in prior work.[25,26] In brief, a gold-coated silicon substrate is rendered hydrophilic through submersion in an aqueous solution (1 mM) of sodium 3-mercapto-1-propanesulfonate (3-MPS) for a minimum of 24 h. The substrate is then near-vertically submerged into a well of the colloidal suspension of monodispersed polystyrene spheres (600 nm sphere diameter, 0.6% w concentration, Thermo Fisher). The thin liquid meniscus on the hydrophilic substrate pulls polystyrene spheres toward the liquid−vapor−solid interface to self-assemble into a crystalline arrangement as the solvent evaporates. A base heating (at 55 °C) promotes gentle convective mixing and prevents sphere sedimentation. The resulting opal template is annealed in an oven (Lab-Line, at 97 ± 0.5 °C for 2 h) to increase the sphere-to-sphere contact area. Copper fills the empty spaces between spheres as the structural material through electrodeposition, using an aqueous electrolyte solution (0.5 M $CuSO_4$ + 0.1 M H_2SO_4). A bulk copper electrode, an opal-covered substrate, and Ag/AgCl serve as the counter, working, and reference electrodes, respectively. An effective current density (of ∼7.5 mA/cm^2; a constant current of 0.875 mA over a total conductive layer area of 0.115 cm^2) is applied in a galvanostatic mode (SP-300, Bio-Logic). The copper−polystyrene composite is immersed in two sequential baths of tetrahydrofuran during which the polystyrene opal template is dissolved. This reveals a copper inverted scaffold of the original opal matrix, where the previous spheres become spherical pore volumes, the sphere-to-sphere contact area becomes interconnected windows between pores (denoted as the "via"), and template cracks become wall-like boundaries. The copper IO is further functionalized in 3-MPS for 24 h to render the structure hydrophilic for capillary wicking.[25] The surface wettability of the functionalized copper IO with DI water and fluorescein fluid is 23.6° ± 5.8° and 26.1° ± 3.2° in static contact angle, respectively. The experimental parameters employed in the IO preparation process directly influence the final IO morphologies and thus can be systematically tuned to vary their physical construction and relevant transport properties. As a result, five sets of IOs with different porosities, degrees of domain anisotropy, and pore-packing qualities are created. Table 1 summarizes the characteristics of each sample, and the following is the variation in the preparation process associated with each sample: sample 1 fabricated using the prescribed conditions above; sample 2 extended the annealing time to 3 h; sample 3 increased the base heating temperature to 80 °C; sample 4 instead of using the vertical deposition technique described above, the colloidal suspension (with higher nanosphere concentration of 5% w) is dropcast onto a substrate heated at 80 °C, which causes rapid self-assembly through sphere sedimentation;[31] sample 5 dropcast colloidal suspension (5% w) on an unheated substrate (room temperature).

Fluorescence Microscopy Imaging of Capillary Transport. The dynamics of in-plane liquid propagation through the polycrystalline IOs are microscopically monitored using a custom-designed setup compatible with the fluorescence microscope (Zeiss LSM700 inverted confocal laser scanning microscope). The moving liquid front is recorded across an area (1070 μm × 1070 μm) with a resolution (1 μm × 1 μm per pixel) at ∼2 Hz. The fluorescein signal is excited at the 488 nm wavelength, and the autofluorescence of the polycrystalline porous copper IO is excited at 639 nm. A custom fixture seals the IO for capillary saturation and is compatible with the inverted fluorescence microscope. The fixture consists of a top and bottom acrylic plate that encloses the PDMS gasket components (PDMS-coated glass coverslip and a molded PDMS top gasket sealer with a channel) and IO samples as secured by fasteners. The PDMS gasket is prepared by mixing SYLGARD-184 base and curing agent (at a 10:1 ratio), followed by degassing in a vacuum desiccator (for 1 h). A thin film of PDMS coats the glass coverslip using a spin coater (at 2000 rpm for 90 s) to produce a film with a thickness (∼50 μm). The molded PDMS top gasket sealer is produced by pouring PDMS into a mold (with a 0.65 mm thick raised slab, similar to the combined height of the IO and its carrier substrate); once cured and removed from the mold, it possesses a rectangular channel that fits the IO sample, and the channel allows the displaced air inside the IO to evacuate during liquid saturation. Both PDMS gasket components (glass coverslip and top gasket sealer) are cured in a lab oven (Lab-Line) at 70 °C for 3 h, and the top sealer is peeled from the mold. For the inverted confocal fluorescence microscope, the top of the IO surface is flipped to face downward and meets the PDMS-coated glass coverslip. The PDMS top sealer aligns its rectangular channel over the IO sample and encapsulates it with the coverslip. The PDMS gasket and IO sample are then sandwiched between the top and bottom acrylic fixture plate. Tightening of the screws across the fixture provides uniform compressive forces to ensure adequate sealing of the IOs. Fluorescein sodium (Sigma-Aldrich) is diluted in DI water by 1 mg/mL. Additionally, fluorescence fluid with higher viscosity is prepared by adding in dextran (2.6 mg/mL) to examine the role of viscosity in porous media liquid propagation. To initiate liquid propagation, the wicking fluid (20 μL) is pipetted onto the PDMS-coated coverslip adjacent to the IOs. The liquid droplet quickly latches onto the sample and is wicked in-plane through the porous medium. The hydrophobicity of the PDMS-coated coverslip prevents liquid wicking across the sealing surface, confines the capillary flow within the IO, and prevents evaporation. Similarly, the hydrophobicity of the PDMS top gasket sealer with a rectangular channel prevents the liquid from flooding the IO while the exit of the channel allows the air from pores to be displaced with minimum impedance during liquid saturation. The wicking fluid is observed as green fluorescence signals when excited with a laser (594 nm wavelength), while the copper IO and its grain boundaries are observed as red signals from its autofluorescence when excited with a laser (639 nm wavelength). See Figure 3, Supplementary Figure 2, and Supplementary Methods for more details.

During image acquisition, the liquid flow is monitored from the inlet (i.e., from the left of the frame) and through its continued propagation across the frame (i.e., to the right). Once the saturation liquid front approaches toward the end of the frame, the stage is mechanically translated laterally to follow the moving liquid front and keep it within the frame. The translation distance and time are noted and incorporated into the propagation distance calculation (Supplementary Figure 3). No data are recorded during camera translation, which contributes to the discontinuities of the plotted propagation results.

Liquid Viscosity Measurement. The shear liquid viscosity is measured using a rheometer (Physica MCR 301, Anton Paar) equipped with a 2° cone and plate geometry (25 mm in diameter) and a truncation gap (52 μm). The viscosities are measured at a controlled temperature (22.5 °C) during the shear ramp test from 0.5 to 100 s^{-1}. See Supplementary Figure 11.

Surface Tension Measurement. The interfacial tension of the liquid in air, γ_{al}, is measured using the pendant drop method. A microsyringe pump (WPI-UMP3 UltraMicroPump) dispenses droplets from the liquid of interest from a syringe connected to a needle tip (30 gauge: 0.31 mm outer diameter, 0.16 mm inner diameter) in ambient air at 22 °C. A high-speed camera (Photron FASTCAM SA8) records the formation of the pendant drop at 2000 Hz, and the shape of the pendant droplet is analyzed using ImageJ software. See Supplementary Figure 12 for representative pendant drop captures and results.

■ ASSOCIATED CONTENT

Supporting Information

The Supporting Information is available free of charge at https://pubs.acs.org/doi/10.1021/acs.langmuir.3c01276.

Additional experimental details, methods, notes, a table, and figures (PDF)

■ AUTHOR INFORMATION

Corresponding Author

Yoonjin Won − *Materials and Manufacturing Technology, University of California, Irvine, Irvine, California 92697, United States; Mechanical and Aerospace Engineering, University of California, Irvine, California 92697, United States; Materials Science and Engineering, University of California, Irvine 92697, United States;* orcid.org/0000-0002-8838-6213; Email: won@uci.edu

Authors

Quang N. Pham − *Materials and Manufacturing Technology, University of California, Irvine, Irvine, California 92697, United States*

Michael T. Barako − *NG Next Basic Research Laboratory, Northrop Grumman Corporation, Redondo Beach, California 90278, United States*

Complete contact information is available at: https://pubs.acs.org/10.1021/acs.langmuir.3c01276

Notes

The authors declare no competing financial interest.

■ ACKNOWLEDGMENTS

This work was sponsored by the National Science Foundation (NSF) (Grant CBET-TTP 1752147, Thermal Transport Processes). Q.N.P. is thankful for the financial support from the UC Irvine Mechanical and Aerospace Engineering Department.

■ REFERENCES

(1) Kim, J.; Ha, J.; Kim, H.-Y. Capillary rise of non-aqueous liquids in cellulose sponges. *J. Fluid Mech.* **2017**, *818*, R2.

(2) Xu, J.; Ji, X.; Zhang, W.; Liu, G. Pool boiling heat transfer of ultra-light copper foam with open cells. *Int. J. Multi. Flow* **2008**, *34*, 1008−1022.

(3) Li, N.; Chen, Z.; Ren, W.; Li, F.; Cheng, H.-M. Cheng, Flexible graphene-based lithium ion batteries with ultrafast charge and discharge rates. *Proc. Natl. Acad. Sci. U.S.A.* **2012**, *109*, 17360−17365.

(4) Chen, Z.; Ren, W.; Gao, L.; Liu, B.; Pei, S.; Cheng, H.-M. Three-dimensional flexible and conductive interconnected graphene networks grown by chemical vapour deposition. *Nat. Mater.* **2011**, *10*, 424−428.

(5) Mendelsohn, J. D.; Barrett, C. J.; Chan, V. V.; Pal, A. J.; Mayes, A. M.; Rubner, M. F. Fabrication of microporous thin films from polyelectrolyte multilayers. *Langmuir* **2000**, *16*, 5017−5023.

(6) Lu, L.; De Hosson, J. T.; Pei, Y. Three-dimensional micron-porous graphene foams for lightweight current collectors of lithium-sulfur batteries. *Carbon* **2019**, *144*, 713−723.

(7) Varrato, F.; Di Michele, L.; Belushkin, M.; Dorsaz, N.; Nathan, S. H.; Eiser, E.; Foffi, G. Arrested demixing opens route to bigels. *Proc. Natl. Acad. Sci. U.S.A.* **2012**, *109*, 19155−19160.

(8) McDevitt, K. M.; Thorson, T. J.; Botvinick, E. L.; Mumm, D. R.; Mohraz, A. Microstructural characteristics of bijel-templated porous materials. *Materialia* **2019**, *7*, 100393.

(9) Zhang, T.; Sanguramath, R. A.; Israel, S.; Silverstein, M. S. Emulsion templating: Porous polymers and beyond. *Macromolecules* **2019**, *52*, 5445−5479.

(10) Kim, S. J.; Choi, J. W.; Moon, M.-W.; Lee, K.-R.; Chang, Y. S.; Lee, D.-Y.; Kim, H. Y. Wicking and flooding of liquids on vertical porous sheets. *Phys. Fluids* **2015**, *27*, 032105.

(11) Nabovati, A.; Llewellin, E. W.; Sousa, A. C. M. A general model for the permeability of fibrous porous media based on fluid flow simulations using the lattice Boltzmann method. *Composites: Part A* **2009**, *40*, 860−869.

(12) Shui, J.; Chen, C.; Grabstanowicz, L.; Zhao, D.; Liu, D.-J. Highly efficient nonprecious metal catalyst prepared with metal-organic framework in a continuous carbon nanofibrous network. *Proc. Natl. Acad. Sci. U.S.A.* **2015**, *112*, 10629−10634.

(13) Zhu, P.; Kong, T.; Tang, X.; Wang, L. Well-defined porous membranes for robust omniphobic surfaces via microfluidic emulsion templating. *Nat. Commun.* **2017**, *8*, 15823.

(14) Herzig, E. M.; White, K. A.; Schofield, A. B.; Poon, W. C. K.; Clegg, P. S. Bicontinuous emulsions stabilized solely by colloidal particles. *Nat. Mater.* **2007**, *6*, 966−971.

(15) Rho, H.; Lee, S.; Bae, S.; Kim, T.-W.; Lee, D. S.; Lee, H. J.; Hwang, J. Y.; Jeong, T.; Kim, S.; Ha, J.-S.; Lee, S. H. Three-dimensional porous copper-graphene heterostructures with durability and high heat dissipation performance. *Sci. Rep.* **2015**, *5*, 12710.

(16) Shin, H.-C.; Liu, M. Copper foam structures with highly porous nanostructured walls. *Chem. Mater.* **2004**, *16*, 5460−5464.

(17) Celebioglu, A.; Uyar, T. Electrospinning of nanofibers from non-polymeric systems: Polymer-free nanofibers from cyclodextrin derivatives. *Nanoscales* **2012**, *4*, 621−631.

(18) Sharstniou, A.; Niauzorau, S.; Ferreira, P. M.; Azeredo, B. P. Electrochemical nanoimprinting of silicon. *Proc. Natl. Acad. Sci. U.S.A.* **2019**, *116*, 10264−10269.

(19) Kamali, S. M.; Arbabi, S.; Kwon, H.; Faraon, A. Metasurface-generated complex 3-dimensional optical fields for interference lithography. *Proc. Natl. Acad. Sci. U.S.A.* **2019**, *116*, 21379−21384.

(20) Zhang, X.; Vyatskikh, A.; Gao, H.; Greer, J. R.; Li, X. Lightweight, flaw-tolerant, and ultrastrong nanoarchitected carbon. *Proc. Natl. Acad. Sci. U.S.A.* **2019**, *116*, 6665−6672.

(21) Guddati, S.; Kiran, A. S. K.; Leavy, M.; Ramakrishna, S. Recent advancements in additive manufacturing technologies for porous material applications. *Int. J. Adv. Manuf. Technol.* **2019**, *105*, 193−215.

(22) Suh, Y.; Pham, Q. N.; Shao, B.; Won, Y. The control of colloidal grain boundaries through evaporative vertical self-assembly. *Small* **2019**, *15*, 1804523.

(23) Suh, Y.; Gowda, H.; Won, Y. In situ investigation of particle clustering dynamics in colloidal assemblies using fluorescence microscopy. *J. Colloid Interface Sci.* **2020**, *576*, 195.

(24) Phillips, K. R.; Zhang, C. T.; Yang, T.; Kay, T.; Gao, C.; Brandt, S.; Liu, L.; Yang, H.; Li, Y.; Aizenberg, J.; Li, L. Photonic Microbricks: Fabrication of Photonic Microbricks via Crack Engineering of Colloidal Crystals (Adv. Funct. Mater. 26/2020). *Adv. Funct. Mater.* **2020**, *30* (26), 2070172.

(25) Pham, Q. N.; Barako, M. T.; Tice, J.; Won, Y. Microscale liquid transport in polycrystalline inverse opals across grain boundaries. *Sci. Rep.* **2017**, *7*, 10465.

(26) Pham, Q. N.; Shao, B.; Kim, Y.; Won, Y. Hierarchical and well-ordered porous copper for liquid transport properties control. *ACS Appl. Mater. Interfaces* **2018**, *10*, 16015−16023.

(27) Wei, B.; Rogers, B. J.; Wirth, M. J. Slip flow in colloidal crystals for ultraefficient chromatography. *J. Am. Chem. Soc.* **2012**, *134*, 10780−10782.

(28) Newton, M. R.; Morey, K. A.; Zhang, Y.; Snow, R. J.; Diwekar, M.; Shi, J.; White, H. S. Anisotropic diffusion in face-centered cubic opals. *Nano Lett.* **2004**, *4*, 875−880.

(29) Barako, M. T.; Sood, A.; Zhang, C.; Wang, J.; Kodama, T.; Asheghi, M.; Zheng, X.; Braun, P. V.; Goodson, K. E. Quasi-ballistic electronic thermal conduction in metal inverse opals. *Nano Lett.* **2016**, *16*, 2754−2761.

(30) Braun, P. V. Materials chemistry in 3D templates for functional photonics. *Chem. Mater.* **2014**, *26*, 277−286.

(31) Lin, N. Y.; Bierbaum, M.; Schall, P.; Sethna, J. P.; Cohen, I. Measuring nonlinear stresses generated by defects in 3D colloidal crystals. *Nat. Mater.* **2016**, *15* (11), 1172−1176.

(32) Yao, X.; Hu, Y.; Grinthal, A.; Wong, T. S.; Mahadevan, L.; Aizenberg, J. Adaptive fluid-infused porous films with tunable transparency and wettability. *Nat. Mater.* **2013**, *12* (6), 529−534.

(33) Galisteo-López, J. F.; Ibisate, M.; Sapienza, R.; Froufe-Pérez, L. S.; Blanco, A.; López, C. Self-assembled photonic structures. *Adv. Mater.* **2011**, *23*, 30−69.

(34) Yang, S.-M.; Jang, S. G.; Choi, D. G.; Kim, S.; Yu, H. K. Nanomachining by colloidal lithography. *Small* **2006**, *2*, 458−475.

(35) Stein, A.; Li, F.; Denny, N. R. Morphological control in colloidal crystal templating of inverse opals, hierarchical structures, and shaped particles. *Chem. Mater.* **2008**, *20*, 649−666.

(36) Armstrong, E.; O'Dwyer, C. Artificial opal photonic crystals and inverse opal structures - fundamentals and applications from optics to energy storage. *J. Mater. Chem. C* **2015**, *3*, 6109−6143.

(37) Lee, Y.-J.; Pruzinsky, S. A.; Braun, P. V. Glucose-sensitive inverse opal hydrogels: Analysis of optical diffraction response. *Langmuir* **2004**, *20*, 3096−3106.

(38) Jin, C.; McLachlan, M. A.; McComb, D. W.; De La Rue, R. M.; Johnson, N. P. Template-assisted growth of nominally cubic (100)-oriented three-dimensional crack-free photonic crystals. *Nano Lett.* **2005**, *5*, 2646−2650.

(39) Wang, L.; Zhao, X. S. Fabrication of crack-free colloidal crystals using a modified vertical deposition method. *J. Phys. Chem. C* **2007**, *111*, 8538−8542.

(40) Hatton, B.; Mishchenko, L.; Davis, S.; Sandhage, K. H.; Aizenberg, J. Assembly of large-area, highly ordered, crack-free inverse opal films. *Proc. Natl. Acad. Sci. U.S.A.* **2010**, *107*, 10354−10359.

(41) Zhou, J.; Wang, J.; Huang, Y.; Liu, G.; Wang, L.; Chen, S.; Li, X.; Wang, D.; Song, Y.; Jiang, L. Large-area crack-free single-crystal photonic crystals via combined effects of polymerization-assisted assembly and flexible substrate. *NPG Asia Mater.* **2012**, *4*, No. e21.

(42) Pham, Q. N.; Zhang, S.; Montazeri, K.; Won, Y. Droplets on slippery lubricant-infused porous surfaces: A macroscale to nanoscale perspective. *Langmuir* **2018**, *34*, 14439−14447.

(43) Zhang, C.; Palko, J. W.; Rong, G.; Pringle, K. S.; Barako, M. T.; Dusseault, T. J.; Asheghi, M.; Santiago, J. G.; Goodson, K. E. Tailoring permeability of microporous copper structures through template sintering. *ACS Appl. Mater. Interfaces* **2018**, *10*, 30487−30494.

(44) Granick, S.; Zhu, Y.; Lee, H. Slippery questions about complex fluids flowing past solids. *Nat. Mater.* **2003**, *2* (4), 221−227.

(45) Ngo, I.-L.; Byon, C. Permeability of microporous wicks with geometric inverse to sintered particles. *Int. J. Heat Mass Transfer* **2016**, *92*, 298−302.

(46) Dusseault, T. J.; Gires, J.; Barako, M. T.; Won, Y.; Agonafer, D. D.; Asheghi, M.; Santiago, J. G.; Goodson, K. E. Inverse opals for fluid delivery in electronics cooling systems. *Fourteenth Intersociety Conference on Thermal and Thermomechanical Phenomena in Electronic Systems (ITherm)*, Orlando, FL; IEEE, 2014; pp 750−755.

(47) Yazyev, O. V.; Louie, S. G. Electronic transport in polycrystalline graphene. *Nat. Mater.* **2010**, *9* (10), 806−809.

(48) Zhang, H.; Yu, X.; Braun, P. V. Three-dimensional bicontinuous ultrafast-charge and -discharge bulk battery electrodes. *Nat. Nano.* **2011**, *6*, 277−281.

(49) Fries, N.; Odic, K.; Conrath, M.; Dreyer, M. The effect of evaporation on the wicking of liquids into a metallic weave. *J. Colloid Interface Sci.* **2008**, *321*, 118−129.

(50) Rogacs, A.; Steinbrenner, J. E.; Rowlette, J. A.; Weisse, J. M.; Zheng, X. L.; Goodson, K. E. Characterization of the wettability of thin nanostructured films in the presence of evaporation. *J. Colloid Interface Sci.* **2010**, *349*, 354−360.

(51) Xiao, R.; Enright, R.; Wang, E. N. Prediction and optimization of liquid propagation in micropillar arrays. *Langmuir* **2010**, *26*, 15070−15075.

(52) Zhu, Y.; Antao, D. S.; Lu, Z.; Somasundaram, S.; Zhang, T.; Wang, E. N. Prediction and characterization of dry-out heat flux in micropillar wick structures. *Langmuir* **2016**, *32*, 1920−1927.

(53) Anbari, A.; Chien, H.-T.; Datta, S. S.; Deng, W.; Weitz, D. A.; Fan, J. Microfluidic model porous media: Fabrication and applications. *Small* **2018**, *14*, 1703575.

(54) Xu, K.; Liang, T.; Zhu, P.; Qi, P.; Lu, J.; Huh, C.; Balhoff, M. A 2.5-D glass micromodel for investigation of multi-phase flow in porous media. *Lap Chip* **2017**, *17*, 640−646.

(55) Krummel, A. T.; Datta, S. S.; Münster, S.; Weitz, D. A. Visualizing multiphase flow and trapped fluid configurations in a model three-dimensional porous medium. *AlChE Journal* **2013**, *59*, 1022−1029.

(56) do Nascimento, D. F.; Vimieiro Junior, J. R.; Paciornik, S.; Carvalho, M. S. Pore scale visualization of drainage in 3D porous media by confocal microscopy. *Sci. Rep.* **2019**, *9*, 12333.

(57) Chu, K. H.; Xiao, R.; Wang, E. N. Uni-directional liquid spreading on asymmetric nanostructured surfaces. *Nat. Mater.* **2010**, *9* (5), 413−417.
(58) Michels, J. J.; Zhang, K.; Wucher, P.; Beaujuge, P. M.; Pisula, W.; Marszalek, T. Predictive modelling of structure formation in semiconductor films produced by meniscus-guided coating. *Nat. Mater.* **2021**, *20*, 68.
(59) Kaviany, M. *Principles of Heat Transfer in Porous Media*; Springer Verlag: New York, 1995.
(60) Ishino, C.; Reyssat, M.; Reyssat, E.; Okumura, K.; Quere, D. Wicking within forests of micropillars. *Europhys. Lett.* **2007**, *79*, 56005−56009.